Structural, electrical and magnetic properties of Co–Cu ferrite nanoparticles

Mohd. Hashim[a,*], Alimuddin[a], Shalendra Kumar[b], B.H. Koo[b], Sagar E. Shirsath[c], E.M. Mohammed[d], Jyoti Shah[e], R.K. Kotnala[e], H.K. Choi[b], H. Chung[f], Ravi Kumar[g]

[a] Department of Applied Physics, Aligarh Muslim University, Aligarh 202002, India
[b] School of Nano and Advanced Materials Engineering, Changwon National University, 9 Sarim Dong, Changwon 641-773, Republic of Korea
[c] Department of Physics, Vivekanand College, Aurangabad 431001, MS, India
[d] Department of Physics, Maharajas College, Ernakulam 682011, Kerala, India
[e] National Physical Laboratory (CSIR), Dr. K.S. Krishnan Road, New Delhi 110012, India
[f] Department of Precision & Mechanical Engineering and BK21 Eco-Friendly Heat & Cooling Energy Mechanical Research Team, Gyeongsang National University, Tongyeong 650-160, Republic of Korea
[g] Centre for Material Science and Engineering, National Institute of Technology, Hamirpur 177005, India

ARTICLE INFO

ABSTRACT

We report structural, electrical and magnetic properties of Cu doped Co ferrite nanoparticles prepared by sol–gel method. Analysis of structural properties has been carried out by using XRD and reveals that all samples have single phase cubic spinel structure. The permittivity (ε), dielectric loss ($\tan\delta$) and ac conductivity (σ_{ac}) were determined at room temperature as a function of frequency. The results of dielectric properties indicated the normal Maxwell–Wagner type dielectric dispersion due to interfacial polarization. Complex impedance spectroscopic studies reveal that the conduction in these samples is through the grain boundaries. Room temperature magnetic hysteresis measurements infer that the saturation magnetization decreases with Cu doping which may be due to the difference of the magnetic moment of Cu and Fe ions.

1. Introduction

Recently, the material science research is focused on the invention of new materials with the enhanced properties and novel synthesis techniques to cope up with the increased technological demand. Nanocrystalline materials are the centre of the attention due to their tremendous applications and interesting properties. The properties of nanomaterials are remarkably different than that of their bulk counterpart. The interest in the ferrite nanoparticles is due to their important physical and chemical properties for various technological applications such as high density magnetic storage, bubble devices, electronic communication devices, sensors, magnetically guided drug delivery [1–3], etc. The major advantages of the ferrite material is that they yield higher efficiency, low cost, and appropriate dielectric loss and hence find potential applications in microwave devices and memory cores [4,5]. Ferrites show the excellent properties when the particle size approaches in the nano range [6]. Cobalt ferrite is a hard magnetic material having cubic spinel structure and attracted considerable attention of the

scientific community due to which it can be used as one of the competitive candidates for specific applications such as high density audio and video recording media, for controlled drug delivery, radio frequency hyperthermia, magnetic resonance imaging (MRI) and medical diagnostics. Because of its moderate saturation magnetization (~80 emu/g) and high coercivity (~5400 Oe), it is used in microwave devices and other high frequency applications [7,8]. Its added features are the chemical stability and mechanical hardness [9–11]. The method of preparation, chemical composition, sintering temperature and duration, grain size, and doping additives play an important role for tailoring properties of spinel ferrites for various applications. Recently, several methods such as spray hydrolysis, sol–gel, co-precipitation, combustion techniques, etc. have been used for prepared the ferrite nanoparticles [12–14]. However, in the present research sol–gel chemistry has been used to prepare the Co–Cu ferrite nanoparticles, as this is simple, low cost and environmental friendly method. Here the mixing of the cations takes place at the molecular level, which gives a very fine, highly dense, homogenous and single phase ferrite at low temperature.

Various groups have studied the effect of doping with different cations to enhance physical properties of spinel ferrites [15,16]. Kumar et al. studied the effect of Ti^{+4} ions doping in Mg–Mn ferrites. They observed that Ti^{+4} doping enhanced the electrical properties

* Corresponding author. Tel.: +91 9359380185.
E-mail address: md.hashim09@gmail.com (Mohd. Hashim).

of Mg–Mn ferrites. Recently, Gautam et al. reported the electronic structure studies of Cu doped cobalt ferrite. They observed that Cu ions occupy octahedral site with +2 valence state [16]. Enhanced magnetic properties of Co–Cu–Zn ferrite were reported by Mane et al. [17]. Cu–Co ferrites for their different properties have been reported in the literature [18–20]. But ac impedance of the crystalline Co–Cu ferrite, which is under investigation, with a chemical formula $CoFe_{2-x}Cu_xO_4$ ($0 \leq x \leq 0.5$) was not well studied and reported in the literature. In the present communication an attempt is made to explore the structural, electrical and magnetic behaviour of $CoFe_{2-x}Cu_xO_4$ ($0 \leq x \leq 0.5$) ferrite nanoparticles. The structural characterization was carried out by X-ray diffraction (XRD), atomic force microscopy (AFM), Fourier transform infrared spectroscopy (FT-IR) and scanning electron microscopy (SEM). Magnetic studies were carried out by using vibrating sample magnetometer (VSM), whereas electrical properties were carried out by using dielectric and ac impedance spectroscopy measurements.

2. Experimental

Different compositions of the $CoFe_{2-x}Cu_xO_4$ ($0.0 \leq x \leq 0.5$) ferrite nanoparticles have been synthesized by sol–gel method. The analytical grade ferric nitrate, cobalt nitrate and copper nitrate (99%, all chemicals were purchased from Sigma–Aldrich) have been used as raw materials. The stoichiometric mixtures of the above materials were dissolved in de-ionized water and few drops of ethyl alcohol were added to it. Few drops of N,N-dimethyl formamide C_3H_7NO (Mw = 73.10) were also added to the solution to get fine crystalline particles. Using a magnetic stirrer and keeping the temperature at 65 °C the solution was constantly stirred until the gel formation. The formed gel was annealed at 200 °C for 24 h followed by half an hour grinding. During this heating the gel self ignites and allow this to continue until the whole gel was burnt out to form a fluffy loose powder. The resultant powder was then heated for 8 h at 800 °C to remove any organic materials present in the sample while maintaining the rate of heating and cooling at 10 °C/min and then the samples were finally ground for half an hour [21]. For electric measurements the samples were pressed into circular disc shaped pellets and silver pasting was applied on the opposite faces to make parallel plate capacitor geometry with ferrite material as the dielectric medium.

X-ray powder diffraction (XRD) patterns have been carried out by using a Rikagu Miniflex (II) with Cu Kα radiation at a sweep rate of 2°/min. The morphological studies were done by using AFM (Digital instruments Nanoscope-IV, with Si_3N_4 100 nm cantilever, 0.58 N/m force constant) measurements in the contact mode. The dielectric and impedance spectroscopy measurements, as a function of frequency at room temperature, were performed by using LCR HI-Tester (HIOKI 3532-50) in the frequency range of 42 Hz to 5 MHz. Fourier transform infrared (FT-IR) spectroscopic analysis was performed by using Jasco model FT-IR 310 spectrophotometer and KBr as a binder. Magnetic measurements have been carried out on a DMS model 880 vibrating sample magnetometer. The permittivity (ε') of the samples has been calculated using the formula:

$$\varepsilon' = \frac{C_p \times d}{\varepsilon_0 A} \tag{1}$$

where C_p is the capacitance of the parallel plate capacitor in F, d is the thickness in cm and A is the cross-sectional area in cm² of the pellet and ε_0 is the free space permittivity. The complex permittivity has been determined using the following relation:

$$\varepsilon'' = \varepsilon' \tan \delta \tag{2}$$

where $\tan \delta$ is the dielectric loss factor which gives the loss of energy from the applied field into the sample (energy dissipated in the form of heat).

The loss tangent ($\tan \delta$) of the materials is related to the resistivity of the sample by this relation:

$$\tan \delta = \frac{1}{2\pi f \varepsilon_0 \varepsilon' \rho} \tag{3}$$

Here f is the frequency of the applied field and ρ is the resistivity.

The ac conductivity of the samples was computed from the following relation:

$$\sigma_{ac} = \varepsilon' \varepsilon_0 \omega \tan \delta \tag{4}$$

where ε' is the permittivity, ε_0 is permittivity of free space (8.854×10^{-12} F/m), ω is the angular frequency and $\tan \delta$ is the loss tangent.
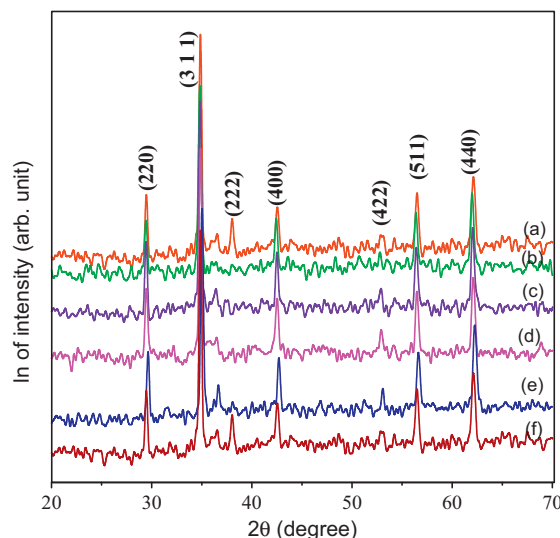

Fig. 1. XRD pattern of $CoFe_{2-x}Cu_xO_4$ ($0.0 \leq x \leq 0.5$) for (a) $x = 0.0$, (b) $x = 0.1$, (c) $x = 0.2$, (d) $x = 0.3$, (e) $x = 0.4$ and (f) $x = 0.5$.

3. Results and discussion

3.1. Structural properties

Fig. 1 shows the X-ray diffraction pattern of $CoFe_{2-x}Cu_xO_4$ ($0.0 \leq x \leq 0.5$) spinel ferrite nanoparticles at 2θ values corresponding to Bragg's reflection which are characteristic features of the single phase cubic spinel structure. All the peaks of the XRD pattern are indexed by JCPDS as reported on ASTM cards (cards 1-1121 and 3-0864). The lattice constant 'a' is determined from the XRD data by using Powder-X-software [22]. The values obtained from the analysis of XRD data lie within the expected range of the lattice constant of spinel cubic ferrites [23]. The variation of the lattice constant with Cu^{2+} doping for various compositions is listed in Table 1. It is seen that the lattice constant increases with increasing concentration of Cu^{2+} ions. The variation in lattice constant may be due to the difference in the ionic radii of the doped ions and the replacing ion. In the present case Fe^{3+} ion is replaced by the Cu^{2+} ion, as the ionic radius of Cu^{2+} ion (0.70 Å) is larger than that of the Fe^{3+} ion (0.67 Å). Since larger ions are replacing smaller ones, an increase in the lattice constant is expected. The average crystallite size (t_{hkl}) of these nanoparticles were calculated from the most intense X-ray diffraction peak (3 1 1) using Scherrer formula [24],

$$t_{hkl} = \frac{0.98\lambda}{\beta_{hkl} \cos \theta_{hkl}} \tag{5}$$

where λ is the X-ray wavelength of the Cu Kα radiation ($\lambda = 1.5406$ Å), θ_{hkl} is the Bragg's diffraction angle and β_{hkl} is the full width at half maximum (FWHM) in radians of the main peak in the X-ray diffraction pattern calculated by using Gaussian fitting.

Table 1
Lattice constant (a), theoretical (D_{tho}) and experimental (D_{exp}) densities, porosity (P), crystallite size (t_{hkl}) of $CoFe_{2-x}Cu_xO_4$.

Comp. x	a (Å)	Densities (g/cm³)		P (%)	t_{hkl} (nm)
		D_{tho}	D_{exp}		
0.0	8.462	3.707	2.755	25.68	29
0.1	8.467	3.655	2.678	26.73	29
0.2	8.469	3.639	2.625	27.86	30
0.3	8.471	3.617	2.599	28.14	30
0.4	8.474	3.596	2.573	28.73	31
0.5	8.477	3.575	2.547	28.75	31

The average crystallite size ranging from 29 to 31 nm for different doping level of copper ion and it is shown in Table 1. The X-ray density (theoretical) is calculated by using the following relation:

$$D_{h\ kl} = \frac{8M}{Na^3} \tag{6}$$

where M is the molecular weight of the compound of ferrite sample, N the Avogadro's number, 'a' lattice constant and 8 represents the number of molecules per unit cell. The apparent density (experimental) of the circular shape pellet is calculated by using the following relation:

$$D = \frac{m}{V} = \frac{m}{\pi r^2 h} \tag{7}$$

where m, V, r and h represent the mass, volume, radius and the thickness of the pellet, respectively. The X-ray density depends on the lattice constant and the molecular weight of the sample, while the theoretical density of the samples is calculated from the geometry and mass of the samples. It can be seen from Table 1, that the X-ray density decreases with Cu^{2+} substitution and the apparent densities of the samples also showed similar behaviour. The higher value of X-ray density than that of the apparent density is due to the existence of pores that depend on the sintering conditions [25]. The porosity of the samples as shown in Table 1, increases with Cu^{2+} substitution; this is due to the lower density of doping ions. Fig. 2(a) and (b) shows the AFM typical micrographs for the sample compositions of $x = 0.0$ and 0.3, where grains of different shapes and sizes are observed.

3.2. Electrical properties

3.2.1. Permittivity

Figs. 3 and 4 represent the variation of real and imaginary parts of permittivity with frequency at room temperature for $CoFe_{2-x}Cu_xO_4$ $(0.0 \leq x \leq 0.5)$ ferrite nanoparticles with different Cu^{2+} composition. It can be seen from Figs. 3 and 4 that as frequency increases both real and imaginary parts of permittivity decrease exponentially. The decrease in both real and imaginary parts of permittivity is rather sharp in low frequency region, as frequency increases it remains almost constant for all the compositions under investigation. The low-frequency dispersion in ferrites is observed due to a space-charge effect [26]. The variation of dielectric constant with frequency reveals dispersion due to Maxwell–Wagner [27,28] type interfacial polarization and is in good agreement with Koop's phenomenological theory [29]. The polarization decreases with increase in frequency and attains constant value beyond certain frequency limit.

The decrease in dielectric constant with frequency indicates that mechanism of polarization process in ferrites is similar to that of conducting process. By electronic exchange, $Fe^{2+} \leftrightarrow Fe^{3+} + e^-$ one obtains the local displacement of electron in the direction of applied field. This displacement determines the polarization in the ferrite. The decrease of the polarization with increasing frequency may be due to the fact that beyond a certain frequency of the electric field the electronic exchange between ferrous and ferric ions cannot follow the alternating field. Hence the dielectric constant decreases substantially as frequency is increased. While investigating the temperature dependence of dielectric properties and resistivity of Ni–Al ferrite Patange et al. suggested two types of charge carriers in ferrite [30]. The n-type charge transfer in ferrites is due to the hopping of electrons from Fe^{2+} to Fe^{3+} ions according to:

$$Fe^{2+} \leftrightarrow Fe^{3+} + e^- \tag{8}$$

while the P-type charge transfer exists in Cu ions according to:

$$Cu^{2+} + h \leftrightarrow Cu^{3+} \tag{9}$$

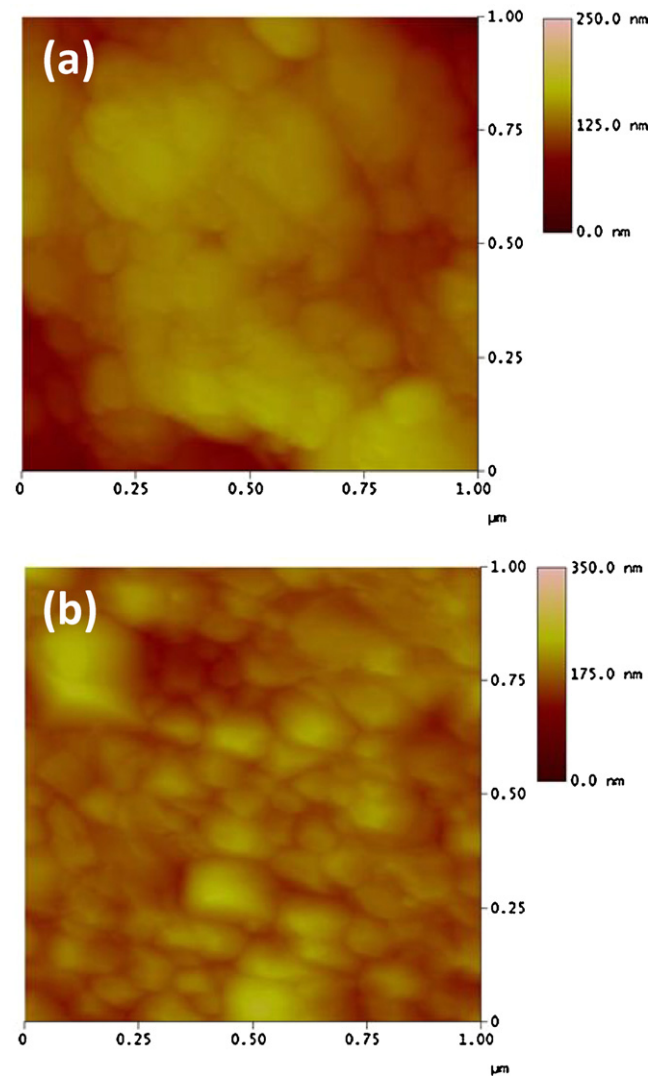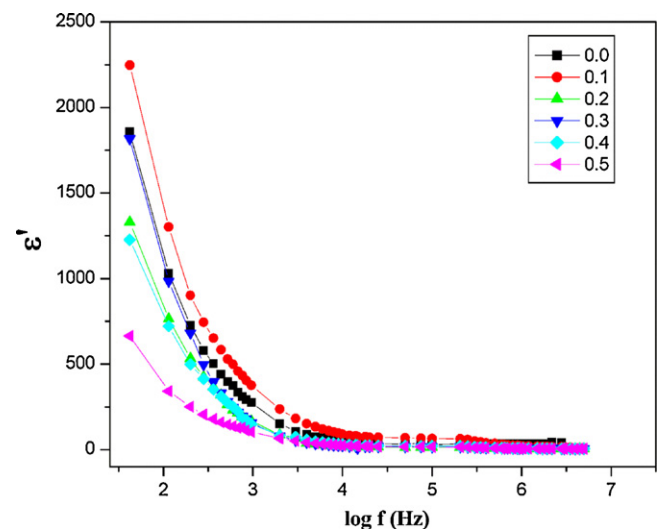**Fig. 2.** AFM of $CoFe_{2-x}Cu_xO_4$ images for (a) $x = 0.0$ and (b) $x = 0.3$.

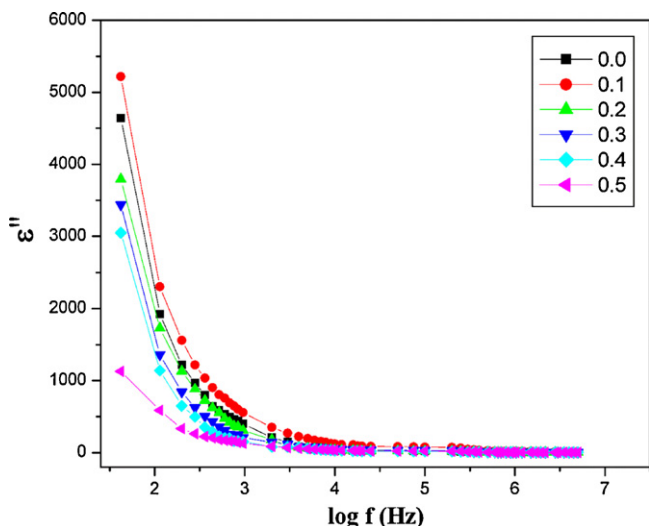**Fig. 3.** Variation of real dielectric constant (ε') as a function of $\log f$ (Hz) of $CoFe_{2-x}Cu_xO_4$.

Fig. 4. Variation of imaginary dielectric constant (ε'') as a function of $\log f$ (Hz) of $CoFe_{2-x}Cu_xO_4$.

The decrease in imaginary part of permittivity is found more pronounced in comparison to the real part of the permittivity. From Fig. 3, it is apparent that the dispersion of dielectric constant is maximum for the sample $x = 0.1$. This maximum dielectric dispersion can be explained on the basis of the number of available Fe^{2+} ions on octahedral sites. In $x = 0.1$, the concentration of ferrous ions is higher than in the other compositions of Co–Cu ferrites at octahedral sites. Therefore, the maximum polarization is possible and it is observed for $x = 0.1$, this results in higher permittivity due to the transfer of electrons between the Fe^{2+}/Fe^{3+} ions.

3.2.2. Dielectric loss tangent

The dielectric loss tangent, $\tan \delta$, determines the energy loss within the ferrite. Dielectric loss arises when the polarization lag behind the applied alternating field which is caused by the impurities and imperfections in the crystal. Fig. 5 depicts the variation of dielectric loss with frequency at room temperature for all the values of x. Anomalous or abnormal dielectric behaviour or relaxation peaks are observed for all the samples. This peaking behaviour is explained by Rezlescu model [31]. According to this model, the peaking behaviour is obtained when the frequency of charge
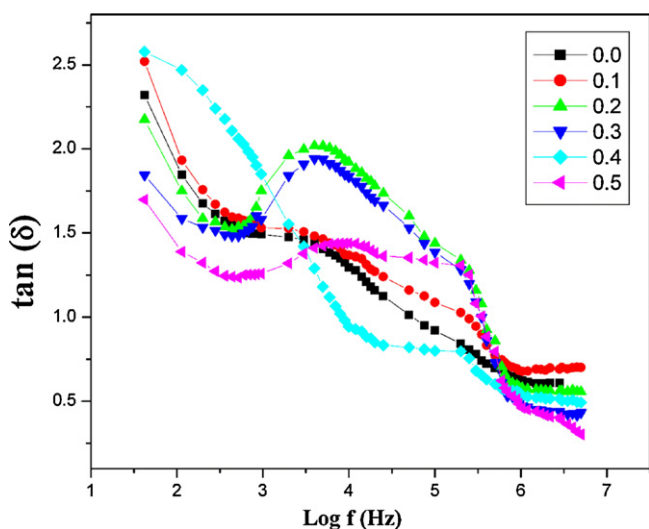

Fig. 5. Variation of dielectric loss tangent ($\tan \delta$) as a function of $\log f$ (Hz) of $CoFe_{2-x}Cu_xO_4$.

hopping between the Fe^{2+} and Fe^{3+} exactly matches with the frequency of the external applied field. The condition for maxima in the dielectric losses of a dielectric material is given by the relation:

$$\omega \tau = 1 \tag{10}$$

where $\omega = 2\pi f_{max}$ and τ is the relaxation time. A relation exits between the relaxation time to the jumping probability per unit time.

$$\tau = \frac{1}{2p} \tag{11}$$

$$\text{or} \quad f_{max} \propto p \tag{12}$$

Therefore, from the above relation it is clear that, maxima is observed when the jumping or hoping frequency of electrons between Fe^{2+} and Fe^{3+} becomes approximately equal to the frequency of the applied field. It is also evident from Fig. 5 that no peaking behaviour is observed for $x = 0.4$ and 0.5. This may be explained on the basis of increasing value of resistivity and decreasing number of Fe^{3+} ions at octahedral site. In the present system, the samples with $x = 0.4$ showed the highest dielectric loss, indicating the favorable condition of hopping between Cu^{2+} and Fe^{3+} ions at octahedral site with the following relation:

$$Fe^{3+} + Cu^{2+} \leftrightarrow Fe^{2+} + Cu^{3+} \tag{13}$$

Fig. 5 also shows that the dielectric loss for all the samples found to be greater at lower frequencies and decreases rapidly with the increase in frequency. This is explained on the basis of the fact that in the low frequency region, which corresponds to high resistivity (due to the grain boundary), more energy is required for electron exchange between Fe^{2+} and Fe^{3+} ions, as a result the loss is high. In the high frequency region, which corresponds to low resistivity (due to grains), a small energy is required for electron transfer between the two Fe ions at the octahedral site. Also at lower frequencies, high dielectric loss may be because of impurities, crystal defects and moisture.

3.2.3. Ac conductivity (σ_{ac}) with frequency

According to Pollak [32] conductivity is an increasing function of frequency if it takes place by hopping of charges and it is a decreasing function of frequency if the band conduction is used. Normally, the whole conductivity is the sum of the band and hopping parts:

$$\sigma_{tot} = \sigma_o(T) + \sigma(\omega, T) \tag{14}$$

where the first term dc conductivity is independent of frequency, which is due to the band conduction. The second term is the pure ac conductivity, which is due to the hopping process at the octahedral site. The frequency dependence of the second term σ_{ac} can be given by the following formula:

$$\sigma_{ac} = B\omega^n$$

where B and n are constants, which depend on both the temperature and composition; n is dimensionless whereas B has the unit of electrical conductivity. Fig. 6 illustrates the variation in $\ln \sigma$ with $\ln \omega$ of nanophase Co–Cu ferrite material of the basic composition $CoFe_{2-x}Cu_xO_4$ ($0.0 \leq x \leq 0.5$) at different frequencies (42 Hz to 5 MHz), at room temperature. It is apparent from Fig. 6 that the ac conductivity shows increasing trend with the frequency for all the compositions. In the low frequency region its value increases linearly according to the power law and in the high frequency region ac conductivity increases gradually, which is the normal expected behaviour of ferrite material. The increase in ac conductivity with frequency can be explained on the basis of Koop's model [29]. According to Koop's model the conductivity at low frequency is due to the existence of grain boundary while the dispersion in the high frequency region is due to the conducting grains. The high density
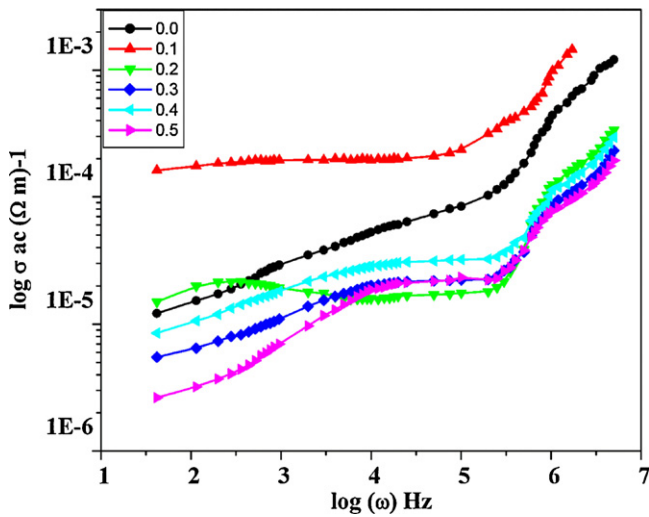
Fig. 6. Variation of ln ac conductivity with $\log\omega$ (Hz) of $CoFe_{2-x}Cu_xO_4$.

Fig. 8. Equivalent circuit representation of impedance plots.

information about the resistive (real part) and reactive (imaginary part) components of the impedance. The plot can give two semi-circles, depending on the electrical properties of the material. The first semicircle in low-frequency region represents the resistance of the grain boundary. The second one obtained for high frequency domain corresponds to the resistance of grain or bulk properties. The impedance spectra can be obtained by using the equivalent circuit consisting of series connecting parallel resistance (R) and capacitance (C) as shown in Fig. 8 [36,37]. The complex impedance of a system at an applied frequency can be written as sum of the real and imaginary part, as follows:

$$Z^*(\omega) = Z'(\omega) + iZ''(\omega) \tag{15}$$

where Z' and Z'' of the impedance can be written as:

$$Z' = \frac{R_g}{(1+\omega_g C_g R_g)^2} + \frac{R_g}{(1+\omega_{gb} C_{gb} R_{gb})^2} \tag{16}$$

$$Z'' = \frac{R_g^2}{1+(\omega_g C_g R_g)^2} + \frac{R_{gb}^2}{1+(\omega_{gb} C_{gb} R_{gb})^2} \tag{17}$$

where R_g and C_g represent the resistance and capacitance of the grain and R_{gb} and C_{gb} represent the corresponding terms for grain boundary, while ω_g and ω_{gb} are the frequency at the peaks of the semicircles for grain and grain boundary, respectively. The resistances are calculated from the circular arc intercepts on the Z' axis, while the capacitances are derived from the maximum height of the circular arcs. The maximum height in each semicircle is $Z' = -Z''$, therefore by using this condition and using above relations, we can calculate the capacitances for grain and grain boundary by using the relations:

$$C_g = \frac{1}{R_g \omega_g} \tag{18}$$

$$C_{gb} = \frac{1}{R_{gb} \omega_{gb}} \tag{19}$$

by using the above two relations the relaxation time for grain and grain boundary were calculated.

$$\tau_g = \frac{1}{\omega_g} = C_g R_g \tag{20}$$

$$\tau_{gb} = \frac{1}{\omega_{gb}} = C_{gb} R_{gb} \tag{21}$$

Fig. 9 shows the complex impedance or Cole–Cole plot (Z' versus Z'') for all the compositions as a function of frequency at room temperature. In the present system, it is clear that only one semi-circular arc corresponding to the conduction due to the grain boundary is obtained, which suggests that a predominant conduction is through the grain boundary volume. Furthermore, contribution from grain is not well resolved in these samples. It is therefore, concluded that the conductivity for all the samples is mainly due to the grain boundaries. The various electrical parameters calculated are shown in Table 2.

of the interfacial states in the nano regime could serve as charge carriers because of ionization and can also function as conduction centres for transport of the charge carriers whereas ac conductivity is at variance with respect to the bulk and the conductivity is found to be higher [33]. The exponent value 'n' calculated as a function of composition for all the samples, by plotting $\ln\sigma$ versus $\ln\omega$ which represents straight lines with slope equal to the exponent n and intercept parts equal to $\ln B$ on vertical axis at $\ln\omega = 0$. Fig. 7 shows the variation of n as a function of Cu^{2+} contents x. It can be noticed from Fig. 7 that the exponent n is found to be composition dependent. It is reported that n has values between 0 and 1. When $n = 0$, the electrical conduction is frequency independent or dc conduction, but for $n \leq 1$, the conduction is frequency dependent or ac conduction [34,35]. In the present ferrite system, the values of the exponent n varies in the range of 0.76–0.81, which suggests that the conduction phenomenon in the studied sample is due to ac conduction.

3.2.4. Complex impedance spectrum analysis

Complex impedance measurements have been used to understand the electrical conduction mechanism of the synthesized ferrite. The complex impedance measurements give the
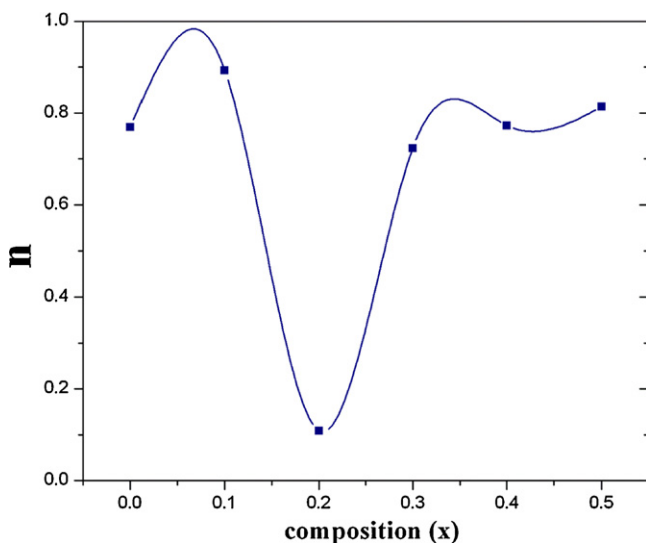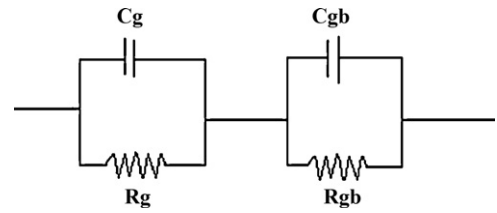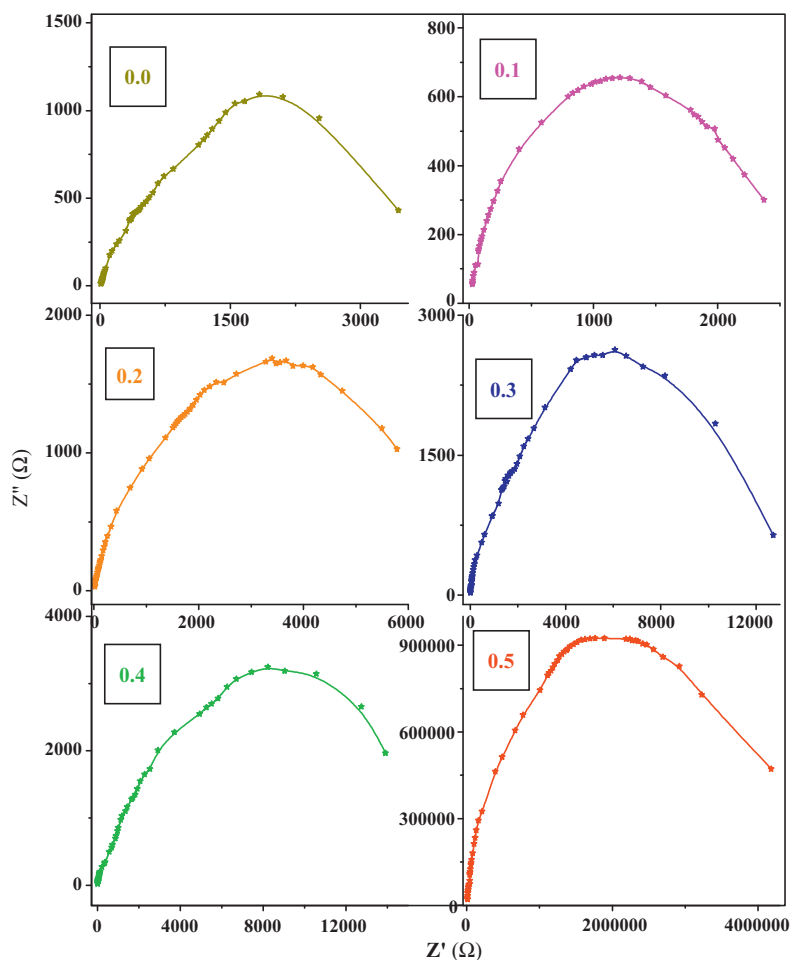

Fig. 7. Exponent value 'n' with Cu concentration of $CoFe_{2-x}Cu_xO_4$.

Fig. 9. Cole–Cole plots of $CoFe_{2-x}Cu_xO_4$.

3.2.5. FT-IR measurement

The vibronic studies using infrared radiation are a good fingerprint for the local chemical bonds. According to Waldron [38], the ferrites can be considered continuously bonded crystals, meaning that the atoms are bounded to all the nearest neighbors by equivalent forces. In spinel ferrites, the metal ions are located into two sub-lattices namely tetrahedral (A-site) and octahedral (B-site) according to the geometrical configuration of the oxygen nearest neighbors. Bands ν_1 and ν_2 are assigned to the intrinsic vibration of tetrahedral and octahedral complexes [38]. The difference in band positions is attributed to the difference in the Fe^{3+} to O^{2-} distances for tetrahedral and octahedral complexes [39]. Fig. 10 shows the IR spectra for $x = 0.0, 0.1, 0.2$ and 0.3. The IR spectra have been used to locate the band positions and their values have been given in Table 3. The higher frequency band (ν_1) is observed at around 595 cm^{-1} and lower frequency band (ν_2) at

around 419 cm^{-1}. The absorption bands observed within this range is an indication of the formation of single phase spinel structure. It has been observed in the present system that the band positions ν_1 and ν_2 changes slightly with Cu^{2+} substitution. This may be due to the distribution of Cu^{2+} ions (ionic radius 0.70 Å), which are
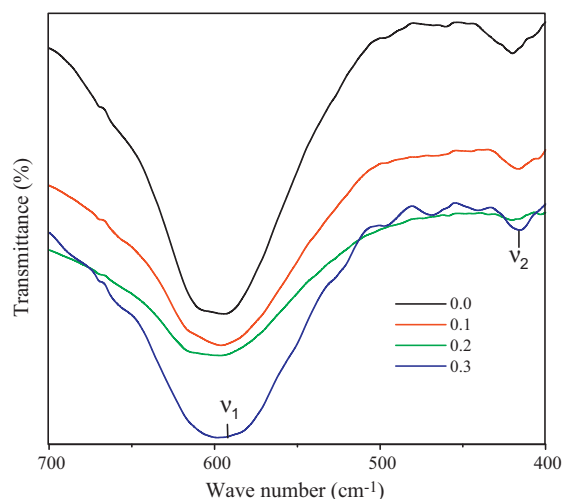
Table 2
Impedance parameters of $CoFe_{2-x}Cu_xO_4$ ferrite nanoparticles at room temperature for grain boundary.

Comp. x	R_{gb}	C_{gb}	τ_{gb}
0.0	3425	2.67E−7	9.00E−3
0.1	2357	6.40E−7	1.50E−3
0.2	5773	1.02E−7	5.93E−4
0.3	12,760	2.90E−8	2.00E−2
0.4	13,891	2.20E−8	3.07E−4
0.5	13,991	3.00E−9	1.08E−4

Fig. 10. Fourier Transform Infrared Spectroscopy of $CoFe_{2-x}Cu_xO_4$ (for $x = 0.0, 0.1, 0.2, 0.3$).

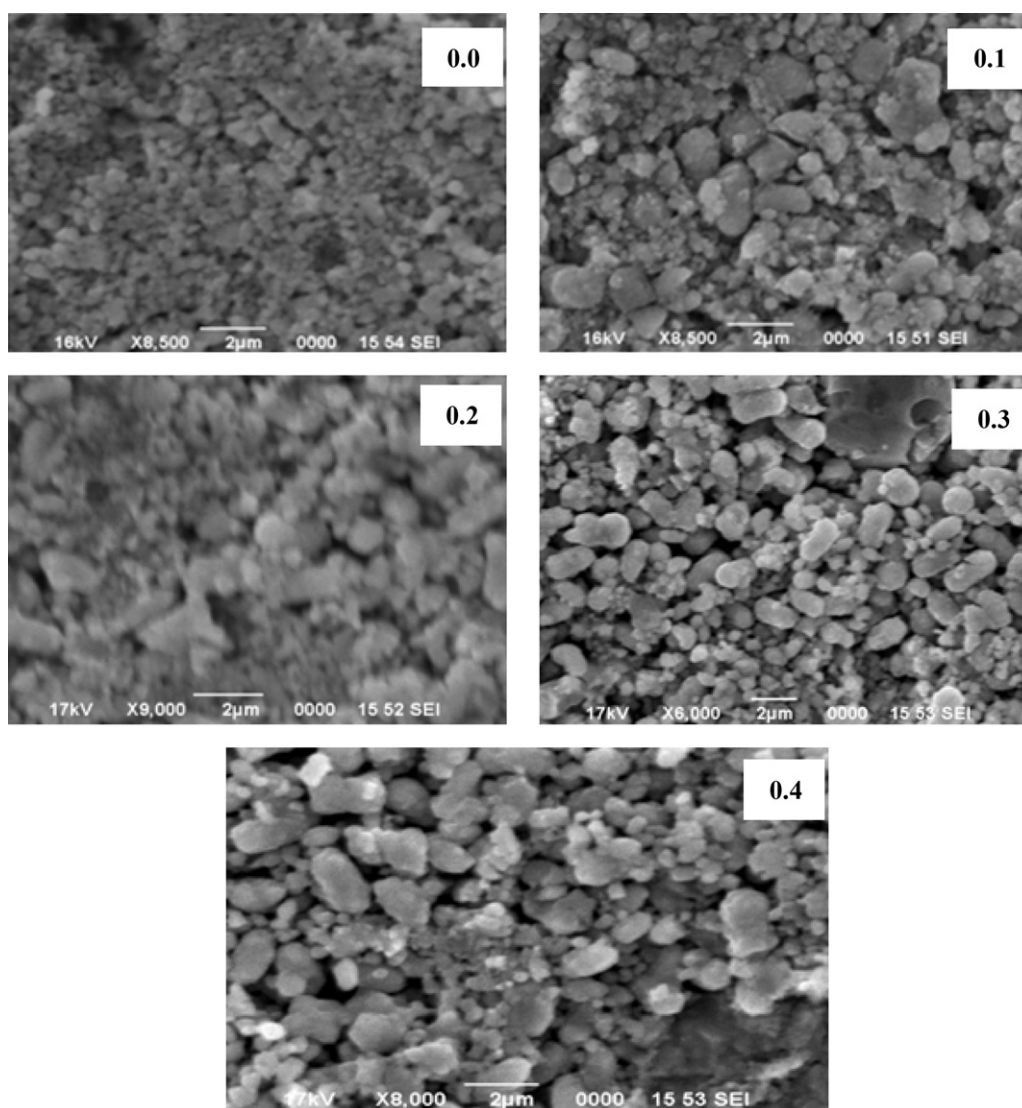**Fig. 11.** Scanning electron micrographs of $CoFe_{2-x}Cu_xO_4$ (for $x = 0.0, 0.1, 0.2, 0.3, 0.4$) ferrite nanoparticles.

replacing Fe^{3+} ions (ionic radius 0.67 Å) at octahedral [B] site, thus, making slight change in the size of octahedron and eventually we observed change in ν_2 band position. Similarly, some of the Cu^{2+} ions also occupy the tetrahedral site, which results a change in ν_1 band position.

3.2.6. Scanning electron microscopy (SEM)

The microstructure of the presently investigated ferrite samples was analyzed by using SEM microphotographs as shown in Fig. 11. It is observed from the figure that the sample without doping shows a homogenous microstructure with small grain size distribution. Fine grain growth is found in all these samples. By a closer look at these

microstructures, it is found that the grains in all these samples are spherical in shape [40]. The grain size increases with the increase of doping ion concentration which may be due to oxygen vacancies and porosity that hampers the grain growth.

3.2.7. Magnetic measurement

Fig. 12 shows the magnetization versus applied field (M–H) curve of the synthesized samples obtained by using a vibrating sample magnetometer (VSM) at room temperature. The parameters such as saturation magnetization (M_s) and coercivity (H_c) were calculated using magnetic hysteresis loop measurements. It is observed that the saturation magnetization decreases with increasing the copper ion concentration. This behaviour can be explained on the basis of Neel's two sub-lattice models [41,42]. In the ideal situation, when the prepared sample grows into a pure inverse type spinel structure with all Co^{2+} ions located in the octahedral sub-lattice, the magnetization per formula unit is represented by the net magnetic moment of that in A- and B-sites. The interactions between tetrahedral (A) and octahedral [B] sub-lattices in the spinel system (AB_2O_4) consist of inter-sublattice (A–B) super-exchange interactions and intra-sub-lattice

Table 3
Infrared bands (ν_1) and (ν_2) of $CoFe_{2-x}Cu_xO_4$.

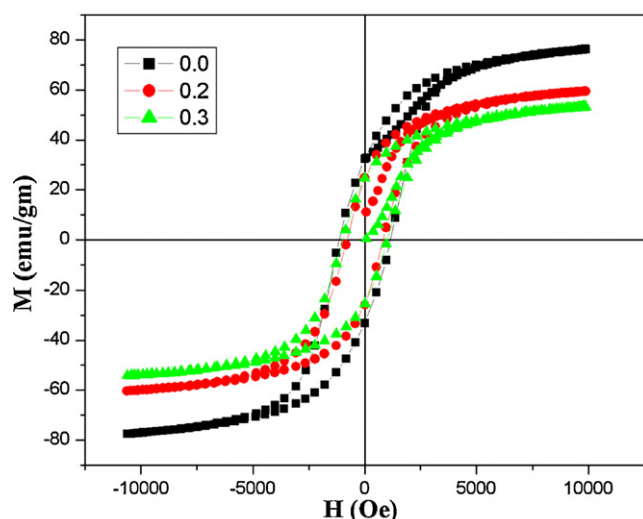| Comp. x	ν_1	ν_2
0.0	595.2	419.26
0.1	595.9	416.91
0.2	596.5	419.15
0.3	596.7	416.24

Fig. 12. M–H curves of $CoFe_{2-x}Cu_xO_4$ (for x = 0.0, 0.2, 0.3) ferrite nanoparticles samples at room temperature.

(A–A) and (B–B) exchange interactions. Inter-sub-lattice super-exchange interactions of the cations on the (A–B) are much stronger than the (A–A) and (B–B) intra-sub-lattice exchange interactions [42]. The preferential occupancy of Co^{2+} ions to the octahedral sites in the ferrite spinel will result in decreasing the concentration of Fe^{3+} ions in these sites, reduce the (B–B) exchange interactions and consequently reduce the (A–B) super-exchange interactions. The magnetic moment can be calculated using the relation, $M_{cal.} = M_B - M_A$, where M_A and M_B represent the total magnetic moment of the A and B sub-lattices, respectively. The magnetic moment of Fe^{3+} cations is fixed to be 5 μ_B (spin only) and that of octahedrally coordinated Co^{2+} cations is fixed to be 3 μ_B. The net magnetic moment for Cu^{2+} has been taken to be 1 μ_B, Cu^{2+} ions having less magnetic moment as compared to those Fe^{3+} ions, so the saturation magnetization is found to decrease with Cu^{2+} doping.

4. Conclusions

X-ray powder diffraction patterns confirm the formation of cubic spinel phase without any additional impurity peaks indicating successful synthesis of $CoFe_{2-x}Cu_xO_4$ ($0.0 \leq x \leq 0.5$) by sol–gel process. The average crystallite size calculated from XRD data was found in the range of 29–31 nm for different Cu^{2+} doping. The dielectric dispersion with frequency is explained on the basis of electron–hole hopping mechanism. FT-IR study confirms two main metal–oxygen bands at $\sim$595 cm^{-1} and $\sim$419 cm^{-1} corresponding to the vibration of the tetrahedral and octahedral M–O bond respectively, confirming the formation of single phase cubic spinel structure of copper doped cobalt ferrite. Analysis of the complex impedance data confirms that capacitive and reactive properties of synthesized materials are mainly attributed due to the processes that are associated mainly with the grain boundary. All the samples show appreciable hysteresis with good value of saturation magnetization at room temperature. The less magnetic moment of Cu^{2+} ions decreases the saturation magnetization of the samples and eventually decreases the A–B interaction.

References

[1] A. Goldman, Modern Ferrite Technology, 2nd ed., Springer, New York, 2006.
[2] N. Sivakumar, A. Narayanasamy, J.-M. Greneche, R. Murugaraj, Y.S. Lee, J. Alloys Compd. 504 (2010) 395.
[3] S.F. Mansour, M.A. Elkestawy, Ceram. Int. 37 (2010) 1175.
[4] I. Soibam, S. Phanjoubam, H.B. Sharma, H.N.K. Sharma, R. Laishram, C. Prakash, Solid State Commun. 148 (2008) 399.
[5] S.A. Mazen, S.F. Mansour, E. Dhahri, H.M. Zaki, T.A. Elmosalami, J. Alloys Compd. 470 (2009) 294.
[6] S.E. Shirsath, R.H. Kadam, A.S. Gaikwad, A. Ghasemi, A. Morisako, J. Magn. Magn. Mater. 323 (2011) 3104.
[7] B.G. Toksha, S.E. Shirsath, S.M. Patange, K.M. Jadhav, Solid State Commun. 147 (2008) 479.
[8] S.S. Jadhav, S.E. Shirsath, S.M. Patange, K.M. Jadhav, J. Appl. Phys. 108 (2010) 093920.
[9] A.T. Ngo, M.P. Pileni, J. Phys. Chem. B 105 (2001) 53.
[10] S. Singhal, J. Singh, S.K. Barthwal, K. Chandra, J. Solid State Chem. 178 (2005) 3183.
[11] M.H. Sousa, F.A. Tourinbo, J. Phys. Chem. B 105 (2000) 168.
[12] S.E. Shirsath, B.G. Toksha, R.H. Kadam, S.M. Patange, D.R. Mane, G.S. Jangam, A. Ghasemi, J. Phys. Chem. Solids 71 (2010) 1669.
[13] Y.I. Kim, D. Kim, C.S. Lee, Phys. B: Cond. Matter 337 (2003) 42.
[14] F. Li, J.J. Liu, D.G. Evans, X. Duan, Chem. Mater. 16 (2004) 1597.
[15] S. Kumar, R. Kumar, P. Thakur, K.H. Chae, S.K. Sharma, Alimuddin, J. Magn. Magn. Mater. 320 (2008) e121–e124.
[16] S. Gautam, S. Muthurani, M. Balaji, P. Thakur, D. Padiyan, Pathinettam, K.H. Chae, S.S. Kim, S.S.A. Asokan, J. Nanotechnol. 11 (2011) 386.
[17] D.R. Mane, D.D. Birajdar, S. Patil, S.E. Shirsath, R.H. Kadam, J. Sol–Gel Sci. Technol. 58 (2011) 70.
[18] A. Bienkowski, Z. Kaczkowski, J. Magn. Magn. Mater. 215–216 (2000) 234.
[19] C. Venkateshwarlu, D. Ravinder, J. Alloys Compd. 426 (2006) 4.
[20] P.P. Hankare, P.D. Kamble, M.R. Kadam, K.S. Rane, P.N. Vasambekar, Mater. Lett. 61 (2007) 2769.
[21] M. Abdullah Dar, K.M. Batoo, V. Verma, W.A. Siddiqui, R.K. Kotnala, J. Alloys Compd. 493 (2010) 553.
[22] C. Dong, J. Appl. Crystallogr. 32 (1999) 838.
[23] A.A. Satar, H.M. El-Sayed, K.M. El-Shokrofy, M.M. El-Tabey, J. Appl. Sci. 5 (2005) 162.
[24] H.E. Schaefer, H. Kisker, H. Kronmuller, R. Wurschum, Nanostruct. Mater. 6 (1995) 533.
[25] M.A. Gabal, S.S. Ata-Allah, Mater. Chem. Phys. 85 (2004) 104.
[26] S.E. Shirsath, S.S. Jadhav, B.G. Toksha, S.M. Patange, K.M. Jadhav, Scr. Mater. 64 (2011) 773.
[27] J.C. Maxwell, Electricity and Magnetism, vol. 2, Oxford University Press, New York, 1973 (Section 828).
[28] K.W. Wagner, Ann. Phys. 40 (1973) 817.
[29] C.G. Koops, Phys. Rev. 83 (1951) 121.
[30] S.M. Patange, S.E. Shirsath, K.S. Lohar, S.S. Jadhav, N. Kulkarni, K.M. Jadhav, Phys. B: Cond. Matter 406 (2011) 663.
[31] N. Rezlescu, E. Rezlescu, Phys. Status Solidi A 23 (1974) 575.
[32] M. Pollak, Proceedings of the International Conference on Physics of Semiconductors, Exeter, 1962, p. 86.
[33] M.G. Chourashiya, J.Y. Patil, S.H. Pawar, L.D. Jadhav, Mater. Chem. Phys. 109 (2008) 39.
[34] M.A. Ahmed, E. Ateia, S.I. El-Dek, J. Mater. Lett. 57 (2003) 4256.
[35] A.L. Hiti, J. Phys. D: Appl. Phys. 29 (1996) 501.
[36] D.C. Sinclair, A.R. West, J. Appl. Phys. 66 (1989) 3850.
[37] J. Ross Macdonald, Impedance Spectroscopy, Wiley, New York, 1987.
[38] R.D. Waldron, Phys. Rev. 99 (1955) 1727.
[39] B.K. Labde, C. Madan Sable, N.R. Shamkuwar, Mater. Lett. 57 (2003) 1651.
[40] Y.-P. Fu, C.-H. Lin, C.-W. Liu, J. Magn. Magn. Mater. 283 (2004) 59.
[41] N.S. Satya Murthy, M.G. Natera, Phys. Rev. 181 (1969).
[42] L. Neel, Ann. Phys. 3 (1948) 137.